Spectrally Matched Quantum Dot Photoluminescence in GaAs-Si Tandem Luminescent Solar Concentrators

Supporting Information

David R. Needell[1], Colton R. Bukowsky[1], Sunita Darbe[2], Haley Bauser[1], Ognjen Ilic[1], and Harry A. Atwater[1†]

† Corresponding Author

[1] Department of Applied Physics, California Institute of Technology, Pasadena, California 91125, United States. Email: haa@caltech.edu

[2] Spiber Inc., 234-1 Mizukami Kakuganji Tsuruoka Yamagata 997-0052, Japan

This document contains 8 pages of supporting information, including 7 figures, 1 table, and 3 equations.

Monte Carlo Ray-Trace Algorithm

We apply a stochastic Monte Carlo ray-trace algorithm in order to closely model designs of luminescent solar concentrator (LSC) with varied luminophore photoluminescence (PL) and absorption profiles [1]. The model takes into account the reflectance, transmittance, and absorbance of the: *(i)* top PL-trapping filter layer, *(ii)* the poly(lauryl methacrylate) (PLMA) waveguide layer with uniformly dispersed quantum dot (QD) luminophores at a waveguide area of 8 mm^2, *(iii)* the embedded and co-planar GaAs micro-cell at a cell area of .16 mm^2, *(iv)* the glass substrate for the GaAs micro-cell, *(v)* the bottom PL-trapping filter layer, and finally *(vi)* the PERC Si subcell. The simulation initializes approximately 10^6 photons across the wavelengths of light 300 nm to 1100 nm, initialized to strike the top surface of the tandem module at normal incidence. The algorithm steps through wavelengths by 10 nm, and integrates all collected photocurrent against the AM1.5g spectrum.

We assume a filter layer coating onto glass substrates for the top and bottom PL-trapping filters with a modeled reflectance profile of a multilayer, one-dimensional stack grating as shown in Fig. S1. In this Monte Carlo simulation, we assume a constant stop-band center for the PL-trapping filters, irrespective of angle of incidence (AoI). Such angular independence can be achieved by filter structures such as high contrast grating (HCG) metasurface and other omnidirectional designs [2]–[6]. We include relatively thin, one micrometer thick, airgaps located between the QD-waveguide and the top/bottom PL-trapping filters. Previous work shows increased PL-trapping by use of such structures in order to collect more photon flux in the embedded solar cell via total internal reflection (TIR) [1], [7]. We assume an average index of refraction of n_{PLMA} = 1.44 for the PLMA layer. Additionally, we follow previous LSC literature with experimentally validated scattering and absorption properties for PLMA [8]. We adjust the concentration of QDs within the PLMA by how strongly the absorption profile adjust the incident solar spectrum, and assign probabilities of photon absorption according to this optical density (OD) of QDs as shown in Fig. S2.

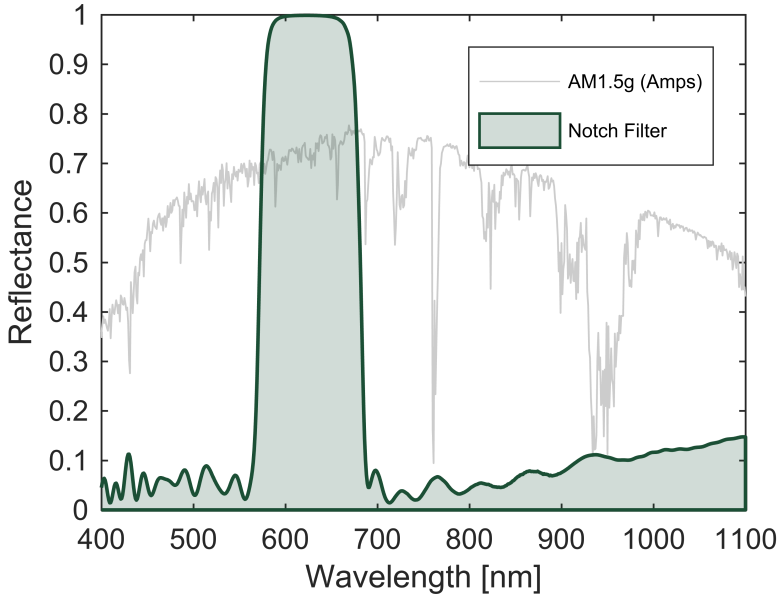

Fig. S1. Reflectance vs. wavelength plot for a simulated, 1 dimensional Bragg stack grating for normal incidence.

We employ the normalized QD PL profile as a probability distribution for photon re-radiation; higher PL radiative efficiency begets higher probability for successful PL at that wavelength. We model the QD absorption/PL profiles from inorganic core/shell CdSe/CdS QDs with experimental measurements shown in Fig. S3 [7], [8]. We then arbitrarily shift the absorption/PL band edges and apply these shifted profiles as independent variables into the Monte Carlo simulation. QDs have shown isotropic absorption

and PL characteristics, and we therefore assign a random direction to every PL event. We apply Snell's and Fresnel's law to every photon as it reaches interfaces between materials of varying index of refraction (e.g. glass, n = 1.5 and PLMA, or glass and air, $n = 1$, etc.).

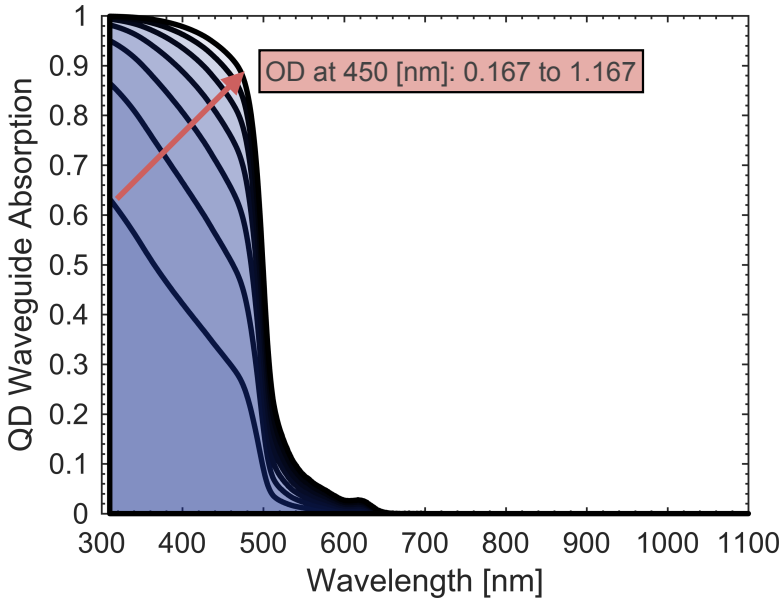

Fig. S2. QD-PLMA waveguide absorption probability for a photon with respect to wavelength and the concentration of QDs within the waveguide. Here we assume a PLMA thickness of 30 micrometers and set the optical density (OD) of the QDs at 450 nm light.

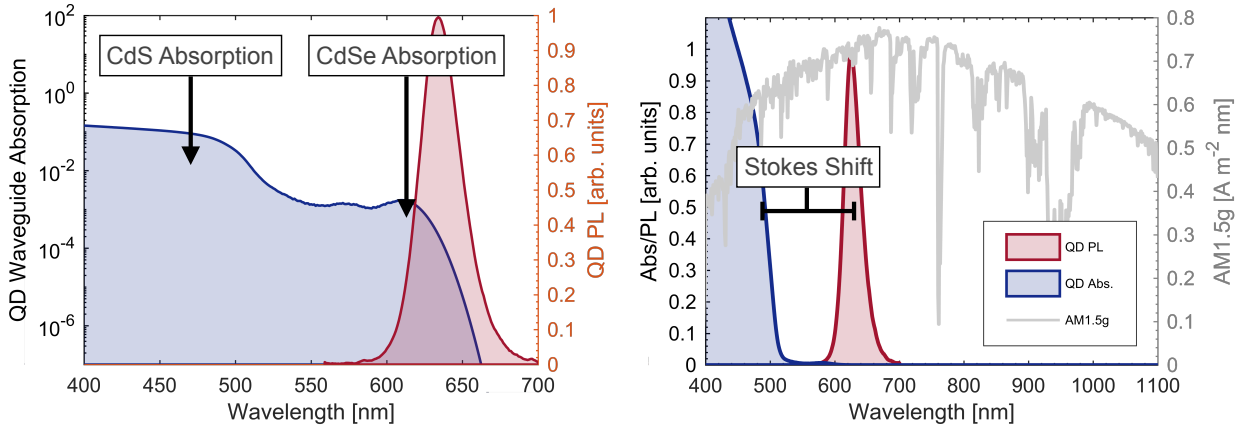

Fig. S3. The spectral characteristics of measured CdSe/CdS QD luminophores for use in a PLMA dispersion. *(left)* The comparison of the absorption (log plot) and PL (linear plot), here the Stokes ratio is the ratio between the QD absorption at the CdS edge to the absorption at the CdSe band edge. *(right)* The comparison between the absorption and PL for the QDs against the AM1.5g incident spectrum.

Finally, we first apply reflection losses to photons incident upon both GaAs and Si cells [9], [10]. If not reflected, we then apply internal quantum efficiency (IQE) to determine which photons are collected as photocurrent and which are lost as heat [9], [10]. Fig. S4 shows the IQE and reflectance curves for each cell [9], [10]. We summarize this Monte Carlo ray-trace algorithm shown in the pseudo-code inset displayed in Fig. S5.

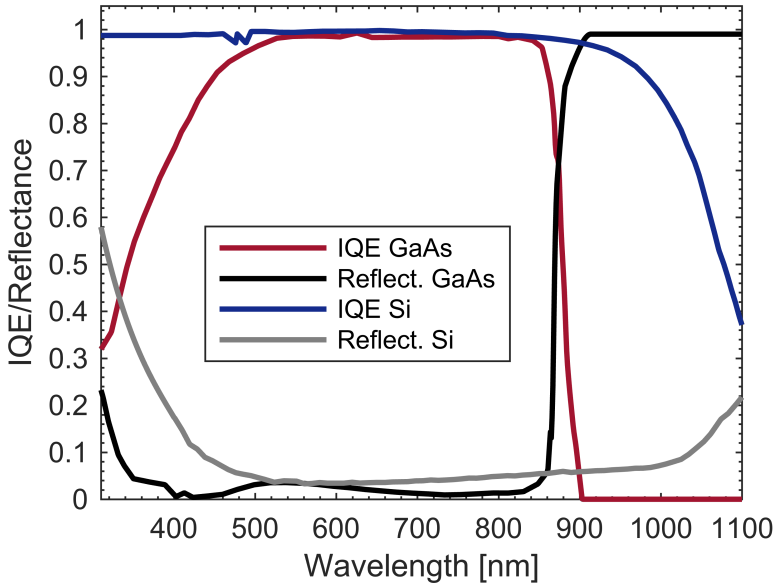

Fig. S4. IQE and reflectance curves for the GaAs and Si cells used in the Monte Carlo ray-trace algorithm ***. We include the wavelength and angle of incidence as inputs to determine successful photocurrent generation from each initialized photon upon reaching either the GaAs or Si cell.

```
initialize LSC Device Geometry
initialize LSC Device Spectral Features
for all applicable wavelengths
     for all grid-points of the LSC
          initialize photon
          if surface reflects/absorbs
               photon lost
          end
          move photon
          if QD absorbs photon
               if QD re-radiates
                    re-radiate photon
                    move photon
               else
                    photon lost
               end
          end
          if hits GaAs
               if not reflected
                    if not lost as heat
                         collect photocurrent
                    else
                         photon lost
               else
                    photon reflected
                    move photon
               end
          end
          if hits Si
               if not reflected
                    if not lost as heat
                         collect photocurrent
                    else
                         photon lost
               else
                    photon reflected
                    move photon
               end
          end
          check boundary conditions
          move photon
     end
end
```

Fig. S5. Monte Carlo ray-trace algorithm pseudo-code showing how the stochastic model treats interactions with LSC components and moves through the device architecture.

Detailed Balance Model

We integrate the collected photocurrent count, determined by the Monte Carlo ray-trace, against the AM1.5g spectrum. We normalize this photocurrent by the total area of the waveguide (i.e. the total illuminated area of 8 mm^2) to achieve a photocurrent density in mA/cm^2. We calculate the open circuit voltage (Voc) for the GaAs and PERC Si cells by taking into account the non-radiative and radiative contributions to the dark current, as shown in supplemental equation (SE) 1.

$$
\begin{aligned}
V_{\mathrm{oc}} &= V_{\mathrm{oc}}^{\mathrm{rad}} + V_{\mathrm{oc}}^{\mathrm{nonrad}} \\
&= \frac{nk_BT}{q} \ln\left(\frac{I_L}{I_0}\right) + \frac{nk_BT}{q} \ln\left(Q_{\mathrm{ERE}}\left(I_L\right)\right)
\end{aligned}
\tag{SE1}
$$

where $V_{\mathrm{oc}}^{\mathrm{rad}}$ and $V_{\mathrm{oc}}^{\mathrm{nonrad}}$ are the radiative and non-radiative contributions to the Voc, n is the ideality factor of the diode equation, k_{B} Boltzmann's constant, q the electron unit charge, I_{L} the total collected photocurrent for the given cell, I_0 the radiative dark current limit, and Q_{ERE} the external radiative efficiency of the cell. We calculate the radiative contribution to the Voc through first principles calculation as shown in SE2. The non-radiative contribution, i.e. the external radiative efficiency of the cell, is modeled via experimental measurements for GaAs [9], [11], [12] and PERC Si [10], [12] cells based upon their EQEs [13].

$$
I_0 = \frac{q}{k_B}\frac{15\sigma}{\pi^4} A_{\mathrm{WG}} T^3 \int_{E_g/k_BT}^{\infty} \frac{x^2}{e^x - 1}\mathrm{d}x
\tag{SE2}
$$

where σ is the Stefan-Boltzmann constant, A_{WG} the area of the illuminated waveguide, T is the temperature of the LSC assumed to be 300K, and E_{g} is the energy bandgap of the cell. We apply Green's method for fill factor (FF) approximation taken from series and shunt resistance values [13]. We empirically match the current-voltage (IV) curve generated via this detailed balance model to measured IV curves for GaAs and PERC Si cells in order to obtain measured resistances [9], [10]. We then apply the FF equation shown in SE3 [14].

$$
\begin{aligned}
\mathrm{FF} &= \mathrm{FF_s}\left(1 - \frac{v_{\mathrm{oc}} + 0.7}{v_{\mathrm{oc}}}\frac{\mathrm{FF_s}}{r_{\mathrm{sh}}}\right) \\
&= \mathrm{FF_0}\left[(1 - 1.1r_{\mathrm{s}}) + \frac{r_{\mathrm{s}}^2}{5.4}\right]\left(1 - \frac{v_{\mathrm{oc}} + 0.7}{v_{\mathrm{oc}}}\frac{\mathrm{FF_0}}{r_{\mathrm{sh}}}\left[(1 - 1.1r_{\mathrm{s}}) + \frac{r_{\mathrm{s}}^2}{5.4}\right]\right) \\
&= \left[\frac{v_{\mathrm{oc}} - \ln\left(v_{\mathrm{oc}} + 0.72\right)}{v_{\mathrm{oc}} + 1}\right]\left[(1 - 1.1r_{\mathrm{s}}) + \frac{r_{\mathrm{s}}^2}{5.4}\right]\left(1 - \frac{v_{\mathrm{oc}} + 0.7}{v_{\mathrm{oc}}}\frac{1}{r_{\mathrm{sh}}}\ldots\right. \\
&\quad \left.\left[\frac{v_{\mathrm{oc}} - \ln\left(v_{\mathrm{oc}} + 0.72\right)}{v_{\mathrm{oc}} + 1}\right]\left[(1 - 1.1r_{\mathrm{s}}) + \frac{r_{\mathrm{s}}^2}{5.4}\right]\right) \\
v_{\mathrm{oc}} &= \frac{V_{\mathrm{oc}}}{nk_BTq}, \quad r_s = \frac{R_s}{V_{\mathrm{oc}}/I_{\mathrm{L}}}, \quad r_{\mathrm{sh}} = \frac{R_{\mathrm{sh}}}{V_{\mathrm{oc}}/I_{\mathrm{L}}}
\end{aligned}
\tag{SE3}
$$

where R_{s} and R_{sh} are the series and shunt resistances for the cell, respectively.

Device Simulation Validation

In order to verify that the Monte Carlo and detailed balance models accurately simulate a realistic LSC component with this device architecture and spectral features, we compare the model against experimentally measured data for the Si PERC subcell and the GaAs cell at full illumination [9], [10], [12]. In addition, we compare this LSC ray-trace against separate and independently verified Monte Carlo ray-trace models [1], [7], [8].

We first simulate a bare Si PERC cell with full illumination under 1-sun, AM1.5g to compare to literature values for efficiency, Voc, and FF. Next, we simulate a full-scale GaAs cell with full illumination under 1-sun, AM1.5g to compare to literature values for efficiency, Voc, and FF. We find the detailed balance model to slightly underestimate Voc for both the GaAs and PERC Si cases; however, we show that the Monte Carlo ray-trace accurately predicts photocurrent within 2% relative error for both the GaAs and PERC Si cases. Table S1 compares these values across literature and LSC Monte Carlo ray-trace modeling. Additionally, Fig. S6 details the Jsc, Voc, and FF for the GaAs and Si micro- and sub-cells, respectively,

for the variation in red-shifting of the luminophore absorption/PL characteristics and corresponding PL-trapping filter stop-band center.

Cell Type	Jsc*	Voc**	FF	Efficiency
Alta GaAs [9]	29.46	1.101	85.76	27.81
Pluto-PERC [10]	39.70	0.670	73.60	19.60
LSC GaAs	29.77	1.074	85.90	27.48
LSC PERC	38.94	0.658	76.70	19.68

* measured in mA/cm^2
** measured in V

Table S1. A comparison between literature GaAs and PERC Si cells under 1-sun, AM1.5g illumination and simulated GaAs and PERC Si cells under the Monte Carlo ray-trace algorithm.

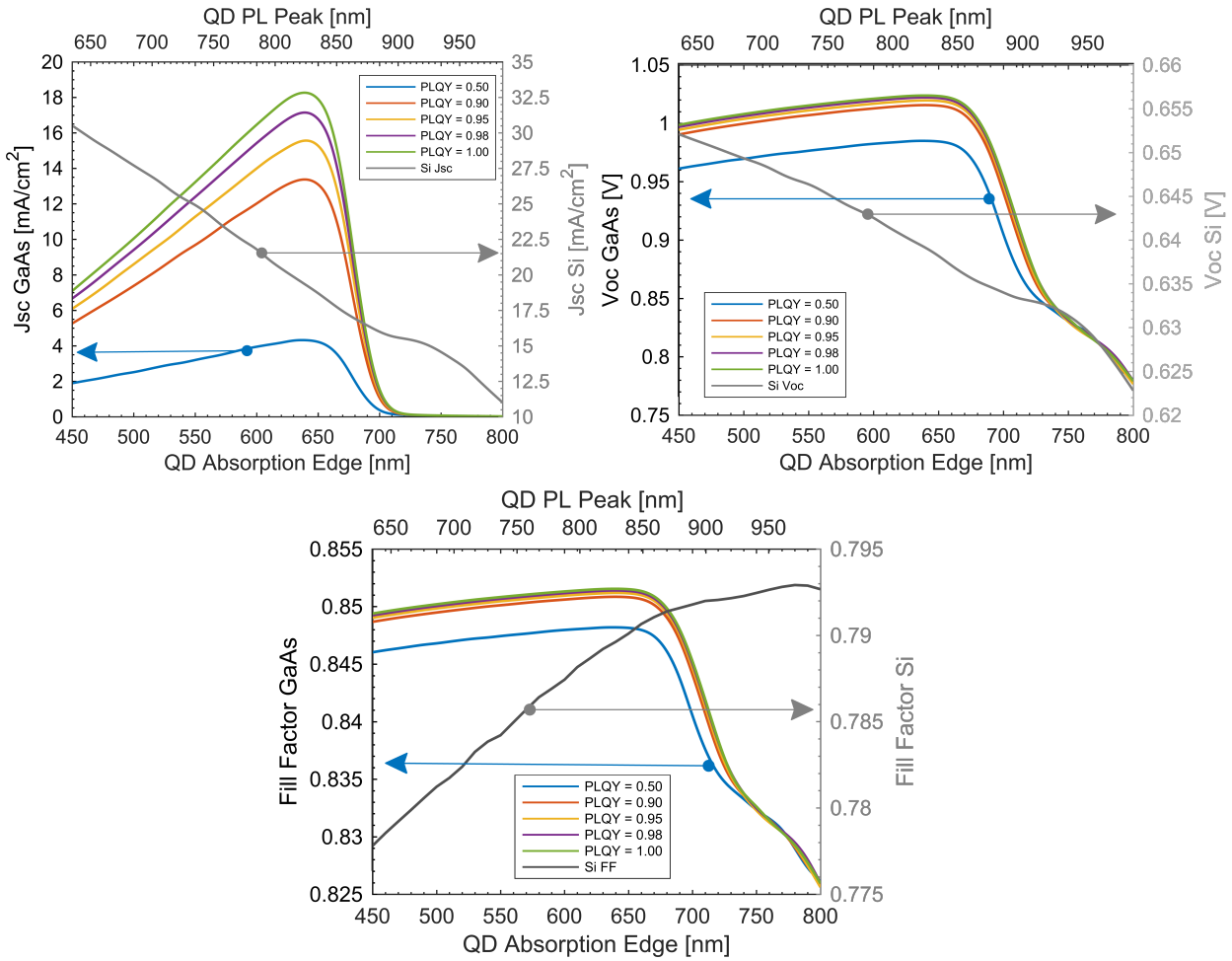

Fig. S6. The effects of luminophore absorption/PL red-shifting on the tandem LSC/Si performance for *(top left)* photocurrent, *(top right)* Voc, and *(bottom)* FF for both the embedded GaAs and bottom PERC Si photovoltaic cells.

Next, we apply this Monte Carlo ray-trace to the study Bronstein et al. conducted to investigate the effects of high PL radiative efficiency of QD luminophores on an LSC structure employing a Si cell [8]. We find matching between the LSC performance when this Monte Carlo ray-trace is used for photocurrent modeling and the experimentally measured values reported by Bronstein et al. Fig. S7 displays the use of

our Monte Carlo ray-trace results to the application and spectral features of the LSC employed by Bronstein et al. [8].

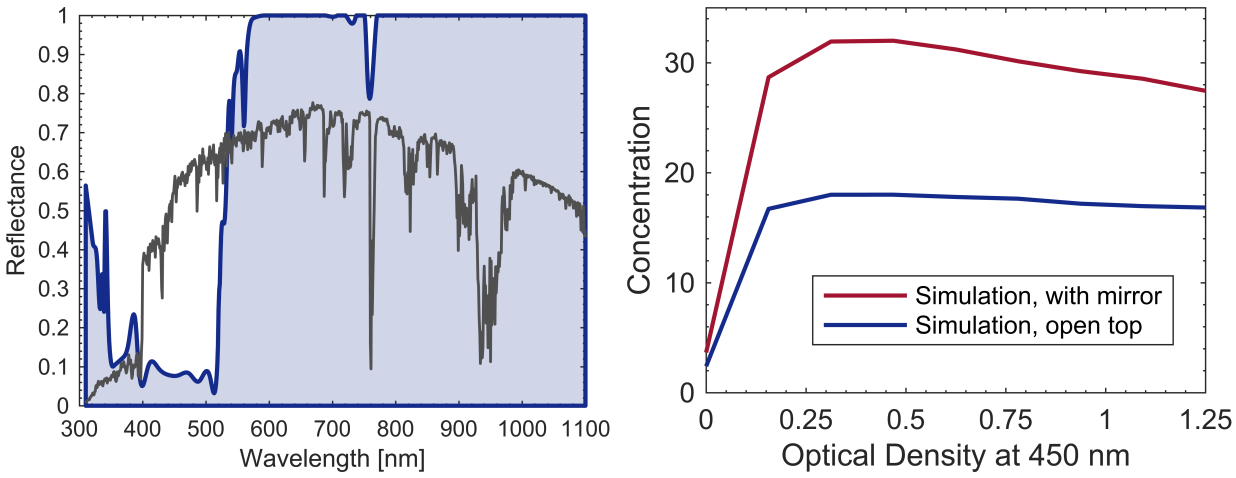

Fig. S7. Monte Carlo ray-trace model validation by direct comparison with the study on high concentration LSC architectures by Bronstein et al. [8]. *(left)* the reflectance spectrum of the short-pass filter employed in that study. *(right)* the concentration vs. optical density measured at 450 nm simulation performed by this ray-trace algorithm used to predict LSC device performance for red-shifting. We observe matching between the above simulation curves and those reported experimentally in [8].

In addition, this Monte Carlo ray-trace has been verified in the study recently released to investigate efficiencies for a tandem LSC-on-Si architecture with baseline CdSe/CdS QDs coupled to InGaP III-V cells in a coplanar format [1].

References

[1] D. R. Needell, O. Ilic, C. R. Bukowsky, Z. Nett, L. Xu, J. He, H. Bauser, B. G. Lee, J. F. Geisz, R. G. Nuzzo, A. P. Alivisatos, and H. A. Atwater, "Design Criteria for Micro-optical Tandem Luminescent Solar Concentrators," *IEEE J. Photovoltaics*, vol. Early Acce, pp. 1–9, 2018.

[2] H. Bauser, D. R. Needell, C. R. Bukowsky, O. Ilic, Z. Nett, B. G. Lee, J. F. Geisz, A. P. Alivisatos, and H. A. Atwater, "Metasurfaces as Wavelength Selective Mirrors in Tandem Luminescent Solar Concentrators," 2018.

[3] A. Arbabi, Y. Horie, M. Bagheri, and A. Faraon, "Dielectric Metasurfaces for Complete Control of Phase and Polarization with Subwavelength Spatial Resolution and High Transmission," *ArXiv*, pp. 1–27, 2014.

[4] V. Karagodsky, F. G. Sedgwick, and C. J. Chang-Hasnain, "Theoretical analysis of subwavelength high contrast grating reflectors," *Opt. Express*, vol. 18, no. 16, p. 16973, 2010.

[5] V. Karagodsky and C. J. Chang-Hasnain, "Physics of near-wavelength high contrast gratings.," *Opt. Express*, vol. 20, no. 10, pp. 10888–95, 2012.

[6] Y. Yao, H. Liu, and W. Wu, "Spectrum splitting using multi-layer dielectric meta-surfaces for efficient solar energy harvesting," *Appl. Phys. A*, vol. 115, no. 3, pp. 713–719, 2014.

[7] D. R. Needell, Z. Nett, O. Ilic, C. R. Bukowsky, J. He, L. Xu, R. G. Nuzzo, B. G. Lee, J. F. Geisz, A. P. Alivisatos, and H. A. Atwater, "Micro-optical Tandem Luminescent Solar Concentrator," in *Photovoltaic Specialist Conference (PVSC), 2017 IEEE 44th*, 2017.

[8] N. D. Bronstein, Y. Yao, L. Xu, E. O'Brien, A. S. Powers, V. E. Ferry, A. P. Alivisatos, and R. G. Nuzzo, "Quantum Dot Luminescent Concentrator Cavity Exhibiting 30-fold Concentration," *ACS Photonics*, p. 150821134054007, 2015.

[9] M. A. Steiner, J. F. Geisz, I. Garc??a, D. J. Friedman, A. Duda, and S. R. Kurtz, "Optical enhancement of the open-circuit voltage in high quality GaAs solar cells," *J. Appl. Phys.*, vol. 113, no. 12, 2013.

[10] Z. Wang, P. Han, H. Lu, H. Qian, L. Chen, Q. Meng, N. Tang, F. Gao, Y. Jiang, J. Wu, W. Wu, H. Zhu, J. Ji, Z. Shi, A. Sugianto, L. Mai, B. Hallom, and S. Wenham, "Advanced PERC and PERL production cells with 20.3% record efficiency for standard commercial p-type silicon wafers," *Prog. Photovoltaics Res. Appl.*, vol. 20, pp. 260–268, 2012.

[11] "Technology Brief - Single Junction GaAs," *Alta Devices*, 2018. [Online]. Available: https://www.altadevices.com/technology/.

[12] M. A. Green, Y. Hishikawa, W. Warta, E. D. Dunlop, D. H. Levi, J. Hohl-Ebinger, and A. W. H. Ho-Baillie, "Solar cell efficiency tables (version 50)," *Prog. Photovoltaics Res. Appl.*, vol. 25, no. 7, pp. 668–676, 2017.

[13] M. A. Green, "Radiative efficiency of state-of-the-art photovoltaic cells," *Prog. Photovolt Res. Appl.*, vol. 20, pp. 472–476, 2012.

[14] M. A. Green, "Accuracy of Analytical Expressions for Solar Cell Fill Factors," *Sol. Cells*, vol. 7, no. 1, pp. 337–340, 1983.